Sensors & Actuators: A. Physical 349 (2023) 114067

Contents lists available at ScienceDirect

Sensors and Actuators: A. Physical

journal homepage: www.journals.elsevier.com/sensors-and-actuators-a-physical

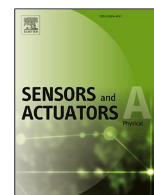

Stress engineering of polycrystalline aluminum nitride thin films for strain sensing with resonant piezoelectric microbridges

M. Schlögl *, J. Weißenbach, M. Schneider, U. Schmid

Institute of Sensor and Actuator Systems, TU Wien, Gußhausstraße 27–29, 1040 Vienna, Austria

ARTICLE INFO

Keywords:
Stress tailoring
Aluminum nitride
MEMS strain sensor
MEMS microbridge resonator

ABSTRACT

For an optimized performance of micro electromechanical systems (MEMS) double-clamped bridge-type resonators for mechanical strain sensing, a modified sputter process was developed which exploits the influence of varying sputter pressure during deposition on the intrinsic stress component of functional thin films. In detail, four different, polycrystalline aluminum nitride layers, synthesized with different sputter parameter sets were characterized related to their microstructure with techniques, such as X-ray diffraction, scanning electron microscopy and atomic force microscopy, respectively. Furthermore, the intrinsic thin film stress and the longitudinal piezoelectric coefficient were evaluated. The best performing layers were integrated in the fabrication process of two MEMS resonant strain sensor devices to study the stress-related impact on the resonant device performance. The initial static buckling of the sensor devices was studied by white light interferometric measurements, whereas the frequency response as a function of externally applied as well as intrinsic strain was analyzed by laser Doppler vibrometry. The behavior of the sensor devices was compared to theoretical predications and the influence of intrinsic thin film stress on the resonance frequency as a function of strain was studied. With a precise tailoring of the intrinsic film stress, a responsivity of ~17000 is measured, representing an improvement by a factor of ~5 compared to state-of-the-art resonant strain sensors.

1. Introduction

Aluminum Nitride (AlN) thin films are widely used as piezoelectric material for MEMS devices due to the compatibility of AlN with complementary metal oxide semiconductor (CMOS) fabrication processes and its outstanding material properties like high temperature stability [1], high breakdown voltage [2] and high electric resistance [2]. Its moderate piezoelectric constant of $d_{33} = 4 - 5pCN^{-1}$ compared to PZT with d_{33} ranging from $50pCN^{-1}$ to $520pCN^{-1}$ [3,4], makes AlN less suitable for actuation purposes but combined with a low permittivity of $\varepsilon_r \approx 10$ (PZT: $\varepsilon_r = 200 - 1500$ [3,4]), AlN excels in sensing applications when exploiting resonance effects as demonstrated in liquids for *e.g.* viscosity measurements [5] or particle monitoring [6,7]. Other applications comprise energy harvesting [8,9], piezoelectric micromachined ultrasonic transducers [10] or surface acoustic wave devices [11]. To increase piezoelectric coefficients, AlN is often alloyed with other elements like scandium, yttrium [12,13], ytterbium [14] or a combination of magnesium and niobium [15], only to name a few dopants.

Beside the piezoelectric properties, another important parameter when targeting MEMS applications is the intrinsic thin film stress. Depending on the deposition technique and the parameters used, the thin film stress in polycrystalline AlN can range from compressive to tensile stress levels [16–18]. Compressive stress can lead to delamination of the thin film during fabrication [19] or warped structures when integrated in mechanically soft structures like microbridges [20] or cantilevers [21,22] where excessive stress can even lead to complete failure of the cantilever, and thus the whole device. Tensile stress can lead to cracking of the thin film [23] which in turn can lead to electrical short circuits given the capacitive structure of the transducer. From a device perspective, thin film stress influences the static bending characteristics of mechanical components [24] as well as the resonance frequency spectrum making it difficult to tune the device to the application-related specifications. As thin film stress may change over time through relaxation, the devices performance is prone to parasitic drift effects [25,26].

Mechanical stress can originate from various sources, *e.g.* lattice mismatch [22,27,28], atomic peening [29] or from different thermal expansion coefficients of substrate and the deposited thin films[30],

* Corresponding author.
E-mail address: matthias.schloegl@tuwien.ac.at (M. Schlögl).

https://doi.org/10.1016/j.sna.2022.114067
Received 19 August 2022; Received in revised form 2 November 2022; Accepted 28 November 2022
Available online 30 November 2022
0924-4247/© 2022 The Authors. Published by Elsevier B.V. This is an open access article under the CC BY license (http://creativecommons.org/licenses/by/4.0/).

occurring either due to temperature loads during fabrication or during temperature variations when operating the device. As AlN additionally often exhibits a stress gradient along the thickness of the thin film [21], a compensation of the overall stress is in some applications not sufficient, so that the stress gradient has to be tuned. Additionally, several publications have reported that tensile stress can increase piezoelectric coupling in AlN thin films [31–34]. Therefore, it is necessary to find ways to reduce the residual stress in AlN thin films, which are discussed in the following.

One way to influence the residual stress of AlN is by varying the thickness of the thin film, as various publications have shown that an increase in thickness can change the overall stress from compressive towards tensile [18,22,35]. But as the MEMS device performance is typically dependent on the overall thickness of the piezoelectric transducer element [36], increasing the latter parameter of AlN thin films might be limited.

Other publications have shown that other sputter parameters also influence the resulting thin film stress, like the substrate temperature during sputtering [22], sputter gas composition [22,37,38] or substrate bias during sputtering [16,33,34].

Several publications have shown that sputter pressure has a great influence on the residual stress in aluminum nitride thin films. In general, increased pressure leads to lower overall stress [39,40], which can be attributed to the decreased kinetic energy of the sputtered particles, due to the reduced mean free path under higher sputter pressure. This reduced kinetic energy also decreases the mobility of the adatoms on the substrate surface [41] and thus reduces the thin film stress. However, the piezoelectric coefficients often decrease in parallel due to the lower crystal quality of the deposited thin films [42,43]. Therefore, when studying the influence of different growth conditions, besides the residual stress, also other material parameters *e.g.* the piezoelectric coefficients, need to be monitored, which often is neglected.

To combine the previous mentioned advantages of different sputter pressures during deposition, Tabaru *et al.* developed an enhanced two step sputter process. This reduces residual stress and simultaneously guarantees high piezoelectric coefficients of ScAlN thin films [44], where managing residual stress is more challenging, due to incorporation of larger scandium atoms into the AlN crystal lattice. While layers sputtered at low pressure showed both very high piezoelectric coefficients and very high compressive stress, thin films sputtered under high sputter pressure resulted in thin films with low stress but also reduced piezoelectric coefficients. Therefore, Tabaru *et al.* tried to combine the advantages of both deposition conditions by sputtering a seed layer with low pressure, followed by a high-pressure sputter step without turning off the plasma during the deposition process. The thin film sputtered during this second step inherits the same crystal orientations as the seed layer but features significantly reduced overall stress. They attribute this effect to atomic peening during the first phase and a selective layer-by-layer adsorption of incoming atoms with lower energy levels during the second phase of the process.

In this work, we focused on the sputter deposition of pure AlN thin films and their influence on piezoelectric resonant microbridges for mechanical strain sensing. Therefore, it is not only important to attain AlN thin films with high piezoelectric coefficients, but also to reduce the residual stress of the whole stack to a minimum to avoid buckling of the microbridges. This was attained by introducing a modified sputter process, whereas the two-step process of Tabaru *et al.* served as reference. Finally, after fabricating several AlN thin films under different deposition conditions for stress reduction they were compared to their compressively stressed counterparts synthesized with a standard sputter process.

2. Sensor principle and theoretical model

The sensor device consists of a microbridge (MB), which is a doubly clamped beam structure and which is excited resonantly. Doing so, resonances or modes form at different frequencies, which depend not only on the resonator design, but also on the externally applied strain, similar to an acoustic guitar where the pitch of the string can be tuned by in- or decreasing the stress through the tuning pegs. The modes have been labeled according to Leissa's nomenclature [45], where the name consists of a two digit number. The first number describes the number of nodal lines along the microbridge's length and the second number corresponds to the nodal lines along the microbridge's width. As we are only discussing classic Euler-Bernoulli modes, which have no nodal line along the width, the second number is always 0. Therefore, the first flexural mode is named "20", the second flexural mode "30" and so on.

Bouwstra *et al.* analyzed the frequency behavior of strained microbridges and developed an analytic expression to predict the frequency changes [46]. In the latter study, the authors started from the Euler-Bernoulli beam equations and the standard equations for unstrained flexural modes (1). Next, they incorporated the dependence on an externally applied force F and hence, the strain ε for a range including a buckled and non-buckled state of the microbridge. The strain value which separates those two states is called buckling point at the strain value ε_C and will be discussed in detail in the results section.

As we are interested in the frequency as a function of strain $f_n(\varepsilon)$ for our devices, we start directly with this dependency and omit the force dependency, where $f_n(0)$ is the resonance frequency of the mode n at zero strain.

$$f_n(0) = \frac{k_n^2}{2\pi}\sqrt{\frac{\hat{E}I}{\rho A l^4}}\forall\varepsilon \geq \varepsilon_C \tag{1}$$

$$f_n(\varepsilon) = f_n(0)\sqrt{1+\gamma_n\frac{\varepsilon E A l^2}{12\hat{E}I}}\forall\varepsilon \geq \varepsilon_C \tag{2}$$

$$\hat{E} = \frac{E}{1-\nu^2} \tag{3}$$

With the moment of inertia for a beam with a rectangular cross section $I = A \bullet h^2 \bullet 12^{-1}$ and $\hat{E}$ being the modified Youngs modulus to account for the suppression of the in-plane dilation accompanying axial strain. The coefficient γ_n accounts for the contribution of the applied axial force to the modal stiffness, relative to the contribution of the flexural rigidity and k_n represent the eigenvalues of the frequency equation for a double clamped Euler-Bernoulli beam [46]. This equation only accounts for values of ε, where the expression below the square root is ≥ 0. The value of ε where the square root is exactly 0 is also called buckling point or critical strain value. At this point the microbridge changes its state from being buckled to being flat or *vice versa*, which will be discussed in more detail below when characterizing the fabricated microbridges. For $\varepsilon < \varepsilon_C$, Bouwstra *et al.* found that the frequency of the first and second flexural mode behave according to (4) and (5), respectively.

$$f_n(\varepsilon) = f_n(0)\sqrt{-\varepsilon/\varepsilon_C - 1}\forall\varepsilon < \varepsilon_C \tag{4}$$

$$f_n(\varepsilon) = 1.98 \bullet f_n(0)\forall\varepsilon < \varepsilon_C \tag{5}$$

with

$$\varepsilon_C = \frac{4\pi^2\hat{E}I}{EAl^2}. \tag{6}$$

Furthermore, center deflections of the unloaded beam z and the loaded beam y are introduced in [46] which have an influence on the frequency close to the critical strain value ε_C as follows:

$$f_n(\varepsilon) = \frac{f_n(0)}{f_0(0)}\sqrt{1+\gamma\frac{\varepsilon E A l^2}{12\hat{E}I} + 0.12\frac{EAy^2}{\hat{E}I}} \tag{7}$$

with

$$y = \frac{z}{1 + \varepsilon/\varepsilon_C}. \quad (8)$$

The values for the material properties used in the model were taken from literature and the geometric dimensions have been determined with scanning electron microscopy analyses for these samples under test. Important parameters can be found in Tables 1 and 2. The averaged values for the Youngs modulus E, the Poisson ratio ν and the density ρ have been related to their thickness according to:

$$X = \frac{h_{Si}}{h}X_{Si} + \frac{h_{AlN}}{h}X_{AlN} + \frac{h_{Au}}{h}X_{Au} + \frac{h_{Cr}}{h}X_{Cr} \quad (9)$$

with X being a placeholder for E, ν or ρ.

When combining Eqs. (7)–(9), the shift in resonance frequency at a given mode is plotted as a function of applied strain and discussed in Fig. 10 together with measurement data of the fabricated devices.

3. Experimental details

3.1. Deposition and characterization of aluminum nitride thin films

AlN thin films were synthesized with a DC magnetron sputter system from “Von Ardenne LS730S” at a temperature below 100 °C on p-type (100) silicon wafers with different parameter sets listed in Table 3. Deposition parameters differ only in the back pressure of the pure nitrogen atmosphere in the sputter chamber while keeping all other parameters fixed such as plasma power, target-substrate distance, or gas flow rate. Within the first and second set constant pressure values of $0.2Pa$ and $0.6Pa$ were selected for a deposition time of $1465s$ and $1928s$. The third and fourth set target to fabricate stress-reduced AlN thin films, whereas the third contained an abrupt change from $0.2Pa$ (for $406s$) directly to $0.6Pa$ (for $1350s$). In contrast, the fourth set consisted of two phases. First, the pressure was kept constant at $0.2Pa$ for $406s$ to create a seed layer. Then the pressure was gradually increased from $0.2Pa$ to $0.6Pa$ over a time period of $1138s$ without interrupting the sputter process. The timings and pressure values for all four sets are depicted in Fig. 1. Additionally, a tailored substrate holder was used to enhance the thermal connection during sputtering between the substrate and the holder as reported in [55,56]. This leads to more reproducible deposition conditions and allows to fine tune stress more reliably. Prior to the thin film deposition, the 6’’ aluminum target was sputter cleaned at a chamber pressure of $0.6Pa$ in a pure argon atmosphere and at a power of $800W$ at the closed shutter for 1 min. For reasons of comparison, all AlN thin films were fabricated with a nominal thickness of $512 \pm 12nm$.

Table 1
List of all parameters used in the model including description, units and values with references when taken from literature.

Parameter	Description	Value	Ref.
E	Youngs modulus (YM)	182 GPa	–
E_{Si}	YM of silicon	169 GPa	[47]
E_{AlN}	YM of AlN	252 GPa	[17]
E_{Au}	YM of gold	69 GPa	[48]
E_{Cr}	YM of chromium	210 GPa	[49]
ν	Poisson Ratio (PR)	0.28	–
ν_{Si}	PR of silicon	0.27	[50]
ν_{AlN}	PR of AlN	0.24	[17]
ν_{Au}	PR of gold	0.42	[51]
ν_{Cr}	PR of chromium	0.21	[52]
$\hat{E}$	Modified YM to account for the suppression of the in-plane dilation accompanying axial strain.	197 GPa	[46]
ρ	density	$5993kgm^{-3}$	–
ρ_{Si}	Density of silicon	$2300kgm^{-3}$	[53]
ρ_{AlN}	Density of AlN	$3100kgm^{-3}$	[54]
ρ_{Au}	Density of gold	$19000kgm^{-3}$	[53]
ρ_{Cr}	Density of chromium	$7190kgm^{-3}$	–
h	MB thickness	$1.57\mu m$	–
l	MB length	$1500\mu m$	–
w	MB width	$100\mu m$	–
z	Center deflection of the unloaded beam	$1.68/21.83\mu m$	–

Table 2
Eigenvalues of the frequency equations k_n, the coefficients γ_n and the frequency ratios of higher flexural modes related to the first flexural mode at zero strain condition according to [46].

n	k_n	γ_n	f_n/f_0
1	4.730	1.000	0.295
2	7.853	2.757	0.145
> 3	$\left(n+\frac{1}{2}\right)\pi$	$\left(\frac{k_n}{4.73}\right)^2$	$12\left(\frac{k_n-2}{k_n^3}\right)$

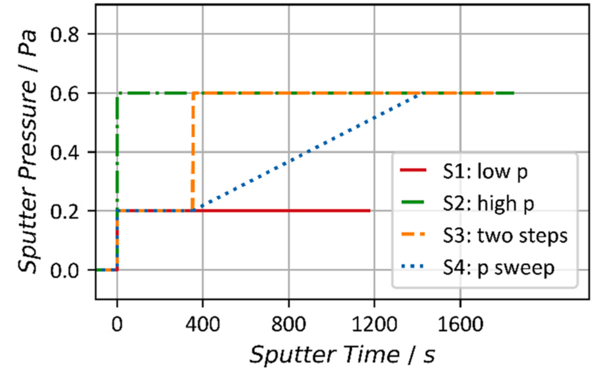

Fig. 1. Pressure variation as a function of time for the AlN thin films sputtered under standard conditions and with modified pressure conditions for stress-reduced thin film synthetization.

Morphological and microstructural characterization of the AlN thin films was done with a Hitachi SU3080 scanning electron microscope (SEM) containing a field emission gun and a secondary electron detector. The images were taken at an acceleration voltage of $3-5kV$ and an emission current of $5mA$. Additional measurements were done with a Brucker Dimension Edge atomic force microscope (AFM) in combination with the scanning probe microscopy data analysis software Gwyddion, to evaluate the surface topography on a scan area of $0.5x0.5\mu m^2$ and to calculate the root mean square of the surface roughness R_{RMS}. The grain size diameter was determined by taking the size of a randomly placed line and dividing it by the number of crossed grains on images taken by SEM and AFM in combination with ImageJ.

The X-ray diffraction (XRD) measurements were performed on a Malver PANanlytical X′Pert PRO. It was equipped with a copper tube operated at 45 kV and 40 mA, with a source to target distance of 140 mm and an X′Celerator detector with an active length of 2.546. For the incident beam a 0.04 rad soller slit, a 2° anti scatter slit and a 0.5° divergence slit were used and the diffracted beam was limited by a 0.04 rad soller slit. Bragg-Brentano scans of all samples were performed within the 2θrange from30°to45°.

The piezoelectric coefficient d_{33} was measured with a piezometer PM300 from Piezotest Ltd. which is based on the Berlincourt method [57]. To decrease the electrical contact resistance between the sample and the electrodes of the piezometer, Al pads with a diameter of $1mm$ were sputter-deposited on the topside, whereas the backside was coated fully with $200nm$ of Al. Nine pads of each sample were measured with a maximum deviation of $\pm 0.5pC\ N^{-1}$.

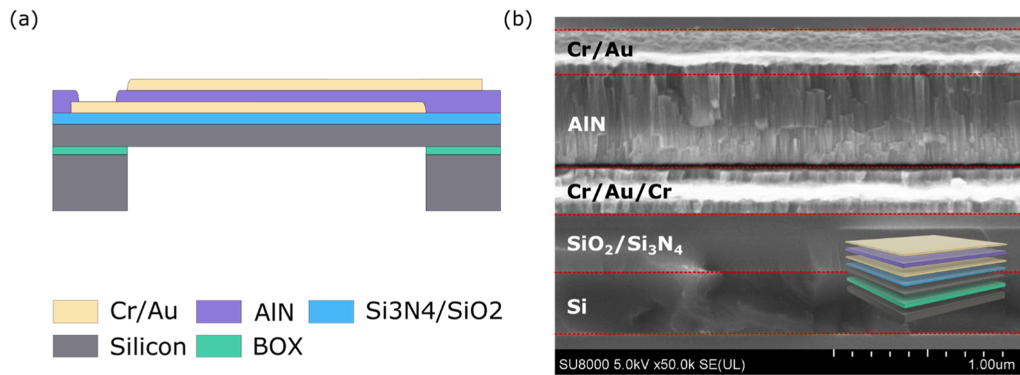

Fig. 2. (a) Schematic overview of the material stack used for the MEMS microbridge resonator. (b) Cross-sectional SEM image of the stacked layers forming the resonating microbridge.

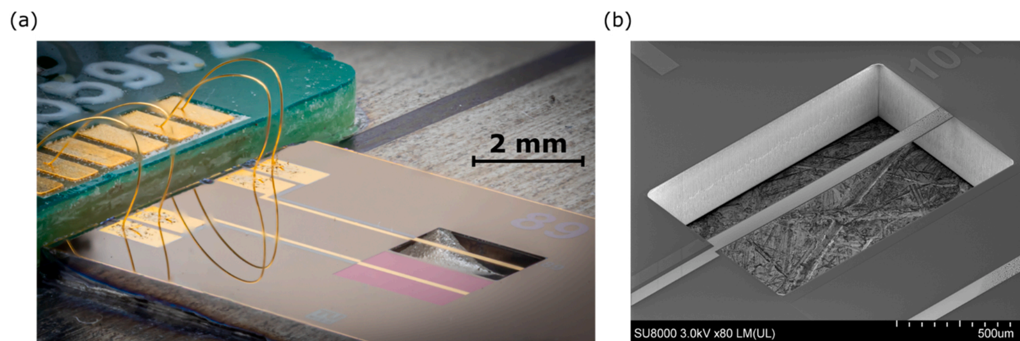

Fig. 3. (a) Optical micrograph of a fabricated and mounted MEMS microbridge resonator, including bond wires and PCBs. (b) SEM image of a MEMS microbridge.

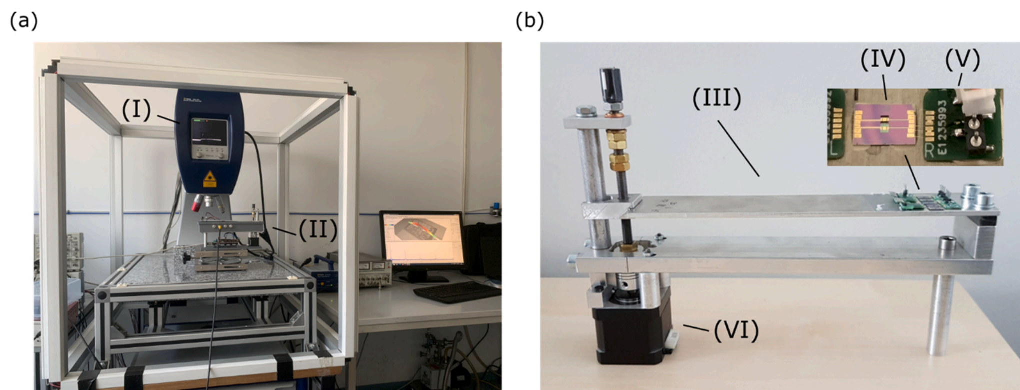

Fig. 4. (a) Optical micrograph of the measurement setup including the LDV (I) and (b) the custom-built strain measurement setup (II) with the bending cantilever (III) and the MEMS sensor device (IV).

The dielectric constant ε_r was calculated from the capacitance measured with a Hioki IM3536 LCR Meter using the same Al pads as described before.

Thin film stress measurements were performed with a MX 203–6–33 wafer geometry gauge from E + H Metrology, which estimates the wafer bow capacitively by determining the distance between the wafer and nine separated counter electrodes at nine different locations. From these data the software calculates according to Stoney`s equation [58], the thin film stress with the actual thin film thickness, which was measured at each sample with SEM.

3.2. Sensor design

The sensor devices were fabricated from a silicon on insulator (SOI) wafer serving as substrate. The SOI wafer has a handle layer thickness of 300μm, a buried oxide (BOX) thickness of 680 nm and a device layer thickness with 330nm. The topside of the device layer was coated with a stress-compensated passivation layer of 230nm silicon oxide and 90nm of silicon nitride. On top of the SOI wafer a conventional stack of bottom electrode, piezoelectric layer and top electrode was deposited as shown in Fig. 2(a-b). The bottom electrode consisted of a 50nm chromium layer and a 150nm gold layer both deposited via electron beam evaporation. The piezoelectric AlN layers were deposited as described above with the low-pressure and the pressure-sweep parameter sets. The other two parameter sets (high-pressure and two-step process) were further investigated, as from pre-investigations the piezoelectric coefficients of these thin films turned out to be too low. Prior to the deposition of the piezoelectric thin film, the aluminum target was in-situ sputtered for

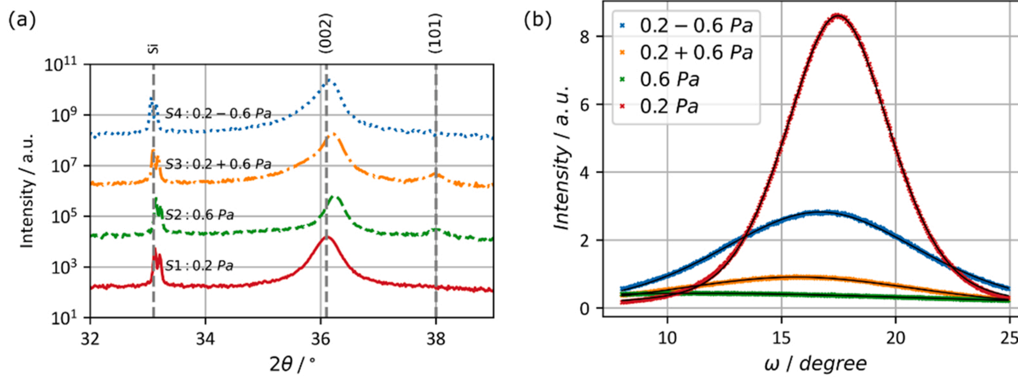

Fig. 5. (a) Bragg-Brentano scans of sputtered AlN thin films with varying sputter pressure. (b) Rocking Curve measurements of the (002)-peak around 36° for each curve in (a).

60 s under pure argon atmosphere for cleaning purposes. The top electrode was realized with the same thicknesses as the bottom electrode. All layers were patterned by a standard lift-off process using photo resist. The handle and device layers were patterned by deep reactive ion etching. To remove the buried oxide and release the microbridge structure an etching step with hydrofluoric acid was performed. The wafer was diced with a wafer saw and the individual chips were cleaned in multiple acetone and isopropanol baths.

The MEMS sensors consist of a microbridge with dimensions of $1500x100x1.6\mu m$. An optical micrograph showing the PCB connected by bond wires is given in Fig. 3(a), whereas a SEM image provides a more detailed view on the microbridge as illustrated in Fig. 3(b). Each chip has been glued onto a test setup and was bonded to PCBs which provide electrical connection for the measurement equipment.

The measurement setup to characterize the sensor device is shown in Fig. 4. To evaluate the device's frequency responses as a function of applied strain ε a laser Doppler vibrometer MSA400 from Polytec (I) was used. The device was excited with the built-in frequency generator, providing a chirp signal generating frequencies from $1kHz$ to $1MHz$ with an amplitude of $0.1V$. The strain ε has been varied by a custom-built strain measurement setup (II), consisting of a bendable cantilever beam (III) made of aluminum. The sensor device (IV) is glued onto the surface of the cantilever beam by an EC101 two component resin from Polytec and connected with wire bonds to self-built PCBs (V) which provide connectors for the frequency generator. If the cantilever is bent down, the sensor strain is tensile in nature, indicated by a positive sign and *vice versa*. The bending is automated via a Nema 17 stepper motor (VI) from Stepperonline which is controlled by an Arduino Mega with a motor driver board which itself can be controlled via a python script from the PC. The spindle which is turned by the stepper motor has a pitch of $1mmrev^{-1}$ and together they provide a resolution of 0.05 revolutions which translates to $50\mu m$ minimum tip displacement of the aluminum cantilever.

4. Results and discussion

4.1. Microstructural and electro-mechanical characterization of AlN thin films

To determine the crystallographic quality Fig. 5 shows the Bragg-Brentano scans of the X-ray diffraction measurements for $2\theta = 30^\circ - 45^\circ$ for all four parameter sets of the sputtered AlN thin films. High quality piezoelectric AlN thin films show a (002) peak indicating a wurtzite crystalline microstructure without the presence of any other peaks e.g., (100) or (101) [59–61].

The thin film sputtered at a chamber pressure of $2\mu bar$ shows a pronounced (002) peak, indicating c-axis oriented crystallites extending perpendicular to the device surface. This is also confirmed by the piezometer measurements showing a d_{33} of $4.14pCN^{-1}$. The crystal growth along the (002) direction in AlN thin films is often accompanied with high intrinsic stress as already described above, in this case shown by a high compressive stress of $\sigma = -722MPa$, which makes the integration in MEMS devices challenging.

In contrast, the sample sputtered with $6\mu bar$ shows a substantially reduced compressive stress of $\sigma = -102MPa$, but also a reduced d_{33} of 0.61 pCN^{-1}. The Bragg Brentano scan shows a (002) peak with reduced intensity and an additional peak at 38.1° indicating the presence of crystallites with a (110) direction. Additionally, a measurement of the rocking curve of the (002)-peak for each of the four curves was performed and shows that the low-pressure sample has the lowest FWHM with 5.44° followed by the pressure-sweep with 10.37°. The other two samples have a very high FWHM of 12.98° and 27.79° for the 2-step-pressure sample and the high-pressure sample, respectively. The Bragg-Brentano scans and the rocking curve confirm the low crystallinity and hence the poor piezoelectric performance of the samples fabricated with higher pressure.

When comparing the two processes selected for stress reduction, we can see that both show a distinct (002) peak but the two step process additionally shows a peak at 38.1° again indicating a mixed crystallographic phase configuration, similar to the sample sputtered with $6\mu bar$. This shows, that while the process with the gentle pressure sweep takes up the crystal structure from the underlying seed layer, in the two step process the crystal growth changes if the sputter pressure is modified abruptly. This impact can also be seen in other film parameters, such as biaxial stress and piezoelectric coefficients. While both processes reduce the compressive stress of the resulting thin film, the two-step process results in a d_{33} of only -1.47 pCN^{-1}, while an enhanced d_{33} of $5.76pCN^{-1}$ is achieved when applying the pressure sweep.

Fig. 6 shows SEM images in cross-sectional as well as in top view of all four differently sputtered AlN thin films. While all four layers show a clear crystal structure in the upper part of the thin film only the low-pressure and the pressure sweep samples show crystal growth starting from the bottom. The high-pressure sample appears to have an amorphous starting layer leading to an irregular growth of grains of about $100 - 150nm$, before developing to the well-known regular, columnar growth in the top part. In contrast, the two-step sample shows a finely grained bottom layer of $148nm$ as intended and a larger grained top layer of $352nm$ with a clearly visible cut between those two layers. The thin film with the pressure sweep shows a very similar structure to the low-pressure sample with grains starting from the bottom and extending over the film cross-section to the top surface.

From the surface images we can see that the high pressure and the two-step sample appear similar and have larger grains with more extended dark areas between the grains, shown in Fig. 6(b) and (c). This originates from the higher surface roughness, which AlN thin films sputtered with higher pressure typically exhibit [62]. The higher surface

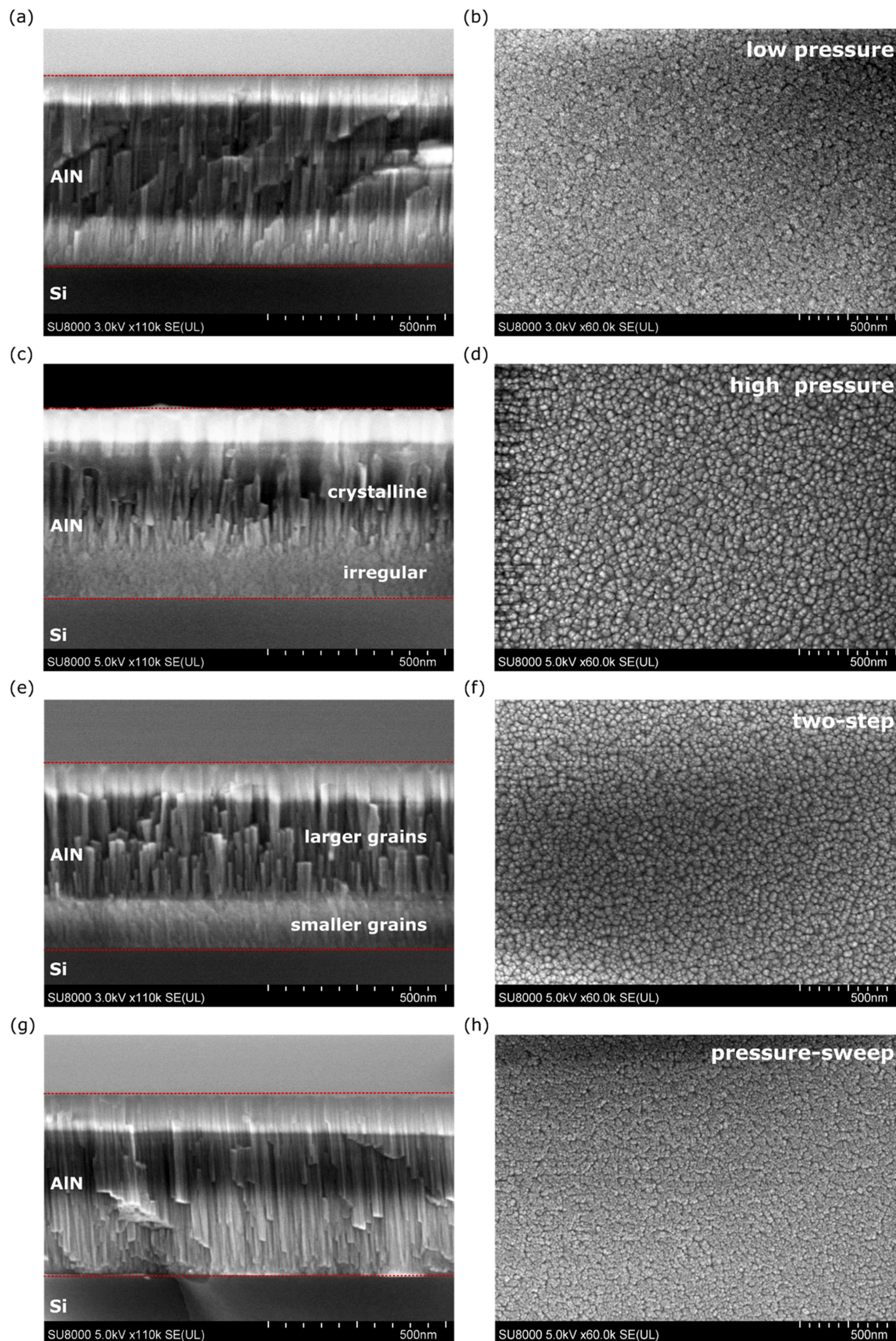

Fig. 6. SEM images of the cross-section and the surface in top view for all four samples sputter with different parameter sets.

roughness is also confirmed by the AFM images in Fig. 7(b) and (d) with $R_{RMS} = 5.12nm$ for the high-pressure sample and $R_{RMS} = 1.98nm$ for the two-step sample. The samples sputtered with low pressure shown in Fig. 6(a) and the pressure-sweep sample shown in Fig. 6(d) also show a similar microstructure with finer grains and less pronounced grain boundaries, which again might result from a lower surface roughness of $R_{RMS} = 0.53nm$ and $R_{RMS} = 0.81nm$ determined by the AFM measurements in Fig. 7(a) and (c), respectively. The attained grain diameters show a similar trend with higher, lateral mean grain diameters with higher scattering variability for the high-pressure sample and the two-step sample than for the low-pressure and the pressure-sweep sample, which are in the expected range according to various published results [59,63,64]. Exact values of the measurements can be found in Table 4. These results confirm the trend of various publications which showed that higher sputter pressure leads to both larger grains and higher surface roughness [59,64,65]. Furthermore, Kar *et al.* who

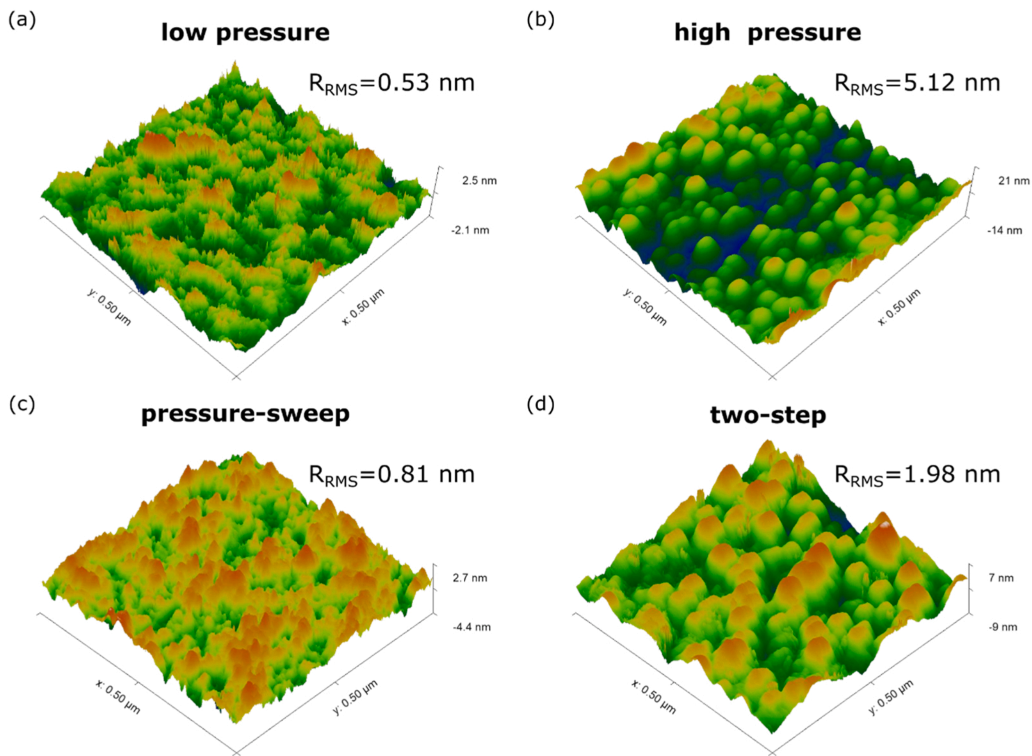

Fig. 7. AFM images of thin films deposited with all four different parameter sets.

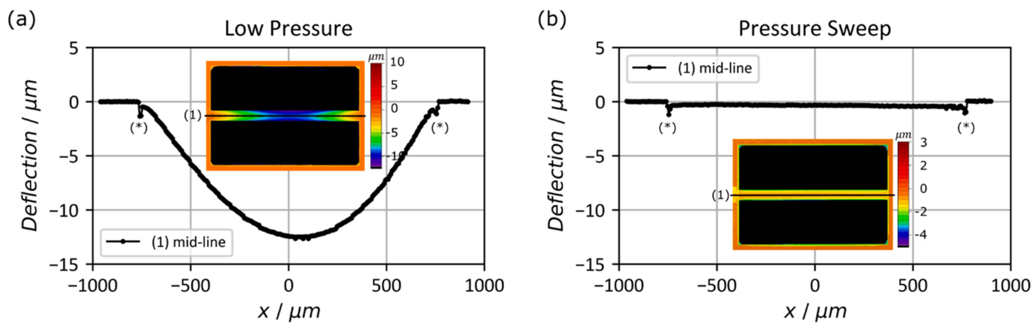

Fig. 8. White light interferometer images and line scans along the microbridge axis for the low-pressure sample (a) and the pressure sweep sample (b).

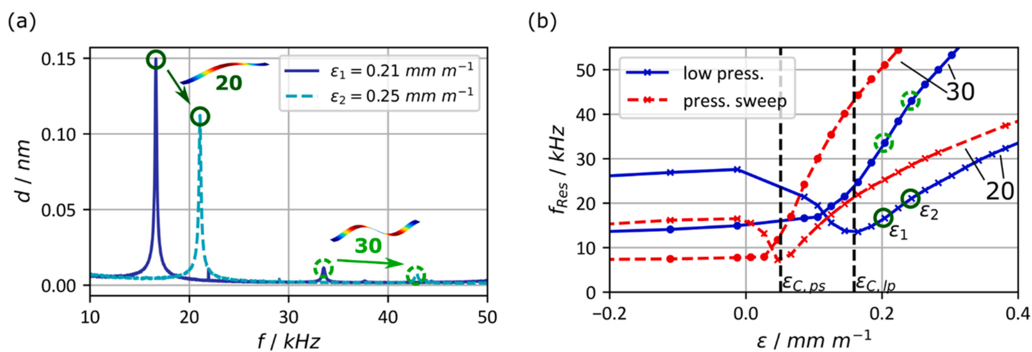

Fig. 9. (a) Two frequency responses of a MEMS sensor device with different externally applied strain values and (b) resonance frequencies as a function of externally applied strain for the first two flexural modes.

studied AlN thin films sputtered under varied sputter pressure showed similar surface structures to our low- and high-pressure samples in their SEM analysis [64].

Table 4 summarizes the measurement results, including XRD measurements, piezoelectric coefficient d_{33}, thin film stress σ, film thickness d_{AlN} and parameters for the surface morphology R_{RMS} and d_{grain}.

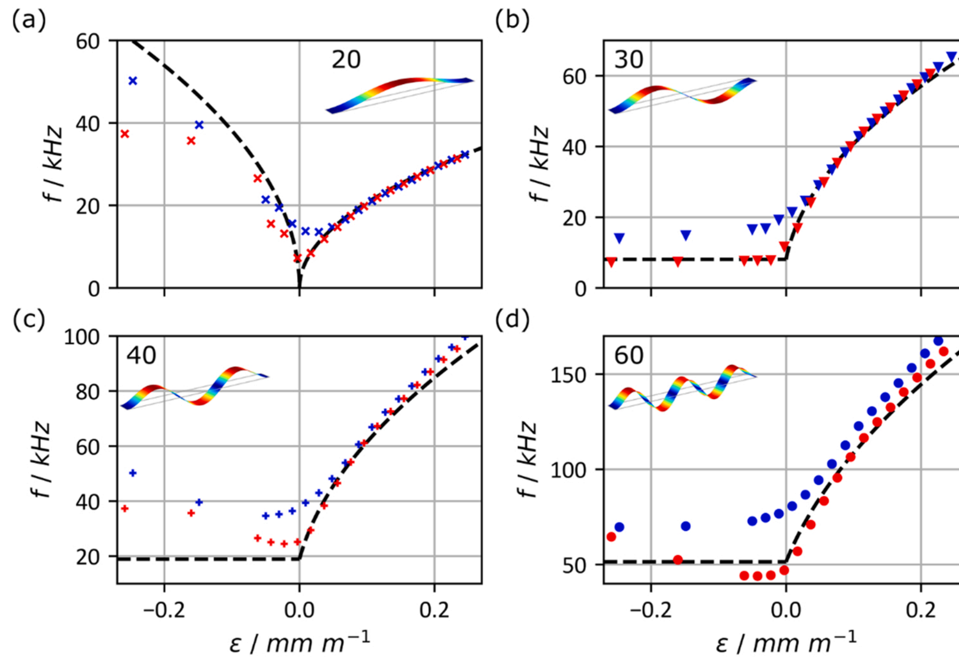

Fig. 10. Comparison of the resonance frequencies as a function of strain for the low pressure (blue) and the pressure sweep (red) device, including the predicted resonance frequencies of the model (black) for the modes (a) 20, (b) 30, (c) 40 and (d) 60.

Table 3
Sputter parameters for AlN thin films deposited for standard conditions and for stress reduced thin films.

	Low Pressure	High Pressure	2 Steps	Pressure Sweep
Sample Nr.	S1	S2	S3	S4
Sputter Pressure / *Pa*	0.2	0.6	0.2 + 0.6	0.2 + 0.2–0.6
N_2 Flow / *sccm*	50	50	50	50
Target Substrate Distance / *mm*	65	65	65	65
Power / *W*	800	800	800	800
Sputter Time / *s*	1465	1928	1756 (406 + 1350)	1544 (406 + 1138)
Thickness / *nm*	523	511	524 (148 + 376)	500 (150 + 350)

Table 4
Various measured parameters of all four AlN thin films.

Wafer	Low Pressure	High Pressure	*2 Steps*	Pressure Sweep
σ / MPa	-722	-102	-389	-170
d_{33} / $pC\ N^{-1}$	4.14 ± 0.3	0.61 ± 0.1	1.47 ± 0.3	5.76 ± 0.5
d_{AlN} / *nm*	523	511	514	500
ε_r	10.4	11.9	11.2	10.8
XRD Intensity	18,973	6224	17,677	23,170
XRD *2θ* / degree	36.079	36.225	36.214	36.161
XRD $FWHM_{RC}$ / degree	5.44	27.79	12.96	10.37
R_{RMS} / nm	0.53	5.12	1.98	0.81
d_{grain} / nm	19.2 ± 3.1	36.6 ± 12.5	32.9 ± 4.2	19.2 ± 3.7

4.2. Sensor characterization

To determine the impact of the developed stress-reduced AlN thin film on device level, fabrication-runs both based on silicon on insulator (SOI) wafers were performed with the two parameter sets, whereas one comprises the low pressure and the second the adapted pressure sweep approach, as described in the Experimental Section.

After fabrication, the devices sputtered with low pressure AlN show buckling with a deflection of the bridge center in the range of $10 - 15\mu m$, as demonstrated by the white light interferometric measurements in Fig. 8(a). In contrast, microbridges where the functional AlN layer is sputtered with the adapted pressure sweep indicate no buckling and remain flat, as depicted in Fig. 8(b). The insets show a 2D scan over the whole surface of the microbridge, while the plotted data represent the line scan along the axis of the microbridge. The irregularities along the line scan marked with a (*) most likely result from phase changes of the reflected white light due to the presence of materials with different optical properties on the surface (i.e. from AlN to Au) [66].

The bottom- and top electrode show a tensile stress of $177MPa$ and $164MPa$, respectively. The residual stress of the full stack can be calculated by the sum of the individual stress values of each layer multiplied by its relative thickness in %. This results in a compressive stress for the low-pressure sample with a value of $-293MPa$ and for the pressure-sweep sample the stress changes to a tensile value of $6.6MPa$, explaining the white-light interferometric measurements with one microbridge being buckled, while the other is not, although both piezoelectric layers are compressively stressed.

The mechanical stress state of the microbridge represented either by a buckled or flat topography has a huge influence on the frequency behavior of the resonator, which will be discussed in the following.

Two frequency response characteristics of the vibrational displacement d, measured with the LDV in the range of $1 - 60kHz$ for the device sputtered with low pressure aluminum nitride for two different externally applied strain values, are shown in Fig. 9(a). The resonances for the vibrational modes 20 and 30 are clearly visible. The frequency values at the resonance peaks are determined, by taking the frequency at the maximum displacement and then they are plotted as a function of strain ε to evaluate the corresponding frequency shifts. Fig. 9(b) shows these frequency values as a function of ε for devices manufactured with both sputtering parameter sets, *i.e.* the low pressure in blue and the pressure sweep in red for the modes 20 and 30. The 20 mode has a frequency minimum f_C at a critical strain value ε_C for which $f(\varepsilon) \geq f_C \forall \varepsilon$. In contrast, the 30 mode shows rising frequency values for $\varepsilon > \varepsilon_C$ and within the measurement accuracy constant frequency values for $\varepsilon < \varepsilon_C$. At this critical strain value, the microbridge changes its state from flat to

buckled. Therefore, we refer to strain values where $\varepsilon < \varepsilon_C$ as buckling regime and for strain values where $\varepsilon > \varepsilon_C$ as the tensile, non-buckling regime. The critical strain values are different for both devices, originating from the different amount of intrinsic compressive stress and hence, from the buckling state after fabrication. The minimum values associated with these frequencies where the critical strain occurs are also different, which will be discussed in more detail later. First, we will analyze the general behavior of the frequency as a function of strain for several modes and compare these findings with the values predicted by the theoretical model.

Fig. 10 shows the resonance frequencies as a function of strain of both devices for the modes 20 in (a), 30 in (b), 40 in (c) and 60 in (d), whereas the 50 mode could not be measured, due to the low signal of this particular resonance. The curves have been normalized so that $\varepsilon_{C,ps} = \varepsilon_{C,lp} = 0$ for reasons of comparison. Additionally, the theoretical predictions given by Eqs. (1) and (2) are inserted. The resonance frequencies of the modes 20 and 30 for both devices overlap for $\varepsilon > 0.05$. For higher order modes, however, the device with higher intrinsic stress give higher resonance frequencies in comparison to the stress-reduced device. Additionally, the deviation of the 60 modes is higher than for the 40 mode, which leads to the assumption that stress has a larger impact on higher order compared to lower order modes. Comparing the model to the measured data we can see that while the model fits nearly perfectly to the data of the 20 mode, the accordance gets worse for higher order modes. A possible explanation for this deviation is the error made with the introduction of γ_n which is a coefficient for the contribution of the applied axial force to the modal stiffness, relative to the contribution of the flexural rigidity and k_n which represents the eigenvalue when solving the frequency equation of an Euler-Bernoulli beam [46]. These values are estimated at zero axial force and neglect effects like shear deformation, dynamic elongation of the beam due to the vibration and different forms of damping, therefore allowing for additional error for higher order modes and higher values of strain, respectively.

For $\varepsilon < -0.05$ the mode shapes are difficult to be identified for two reasons, mode veering and the influence of the static buckling deflection onto the dynamic vibrational displacement.

Mode veering refers to an effect where the resonance frequencies of two modes approach each other, but instead of crossing, they stay separated but exchange their mode shape [67,68]. In this exchange zone, which is also called transition zone, the typical mode labeling convention cannot be applied due to the irregular mode shape patterns, when regular modes exchange their mode shape [69,70]. In Fig. 10 we can already see that the model predicts such transition zones in the buckling regime, whenever the 20 mode crosses other modes.

The other interfering effect is the static buckling deflection resulting from the external applied strain or the intrinsic thin film stress. When the microbridge resonates, the dynamic vibration is superposed onto the static deflection, resulting in a non-regular mode shape [71–74]. As the buckling deflection gets larger the further we strain the microbridge into the buckling regime, the more the measured mode shapes get distorted, leading to difficulties in assigning the right modes.

For the strain range $-0.05 < \varepsilon < 0.05$ the first and second flexural mode are investigated separately, as depicted in Fig. 11(a-b). The 20 mode of the pressure sweep sample has lower frequency values around and at ε_C, than the low-pressure sample. This has been explained in the model of Bouwstra *et al.* by an initial deflection z, which shifts the value of the frequencies around ε_C to higher values (compare Eq. (7)). Although, their extended model which includes the initial deflection shows the same behavior like our microbridges qualitatively, the model is only valid in a very narrow range around ε:

$$-1.3 < \frac{\varepsilon}{\frac{4\pi^2 \hat{E}I}{EAl^2}} < 1. \tag{10}$$

As our data suggests that the influence of the initial buckling is much stronger than predicted by the model, we could not fit the data to the extended model.

For $\varepsilon < -0.05$ both curves seem to approach the model as far as this can be evaluated due to the difficulties of identifying the modes as described before. For the 30 mode the same behavior as for the 20 mode is around ε_C. For $\varepsilon < -0.05$ the pressure-sweep sample approaches $\sim 8kHz$ which is in good agreement with the model, whereas the low-pressure sample approaches $\sim 18kHz$. This deviation indicates that the modeled initial deflection is not sufficient to explain all effects of thin film stress, especially in the buckling regime.

For higher modes we can see that in the non-buckling regime the data for the two different devices increasingly diverges from the model with increasing mode order. In the buckling regime we see a similar behavior, but due to mode veering it is even more difficult to estimate the correct frequency behavior and to give proper explanations.

4.3. Responsivity

As the microbridge is initially buckled after fabrication, which shifts ε_C towards higher values of ε compared to unbuckled microbridges, the initial working point ε_{WP} is in the buckled regime of the sensor device which is not suitable for strain sensing as the frequency is ambiguous when crossing ε_C. One way to circumvent this is by pre-straining the device when mounting it to the structure under test or during packaging, both challenging tasks. Obviously, another way is to adapt the thin film stress in a way that ε_C is modified such that its working point is set to a desirable value.

With this said, we can define the relative responsivity of the sensor device, as the slope of $f(\varepsilon)$ related to the base frequency f_0 at ε (Eq. (11)).

$$R = \frac{\Delta f}{f_0 \varepsilon} \tag{11}$$

Fig. 12(a) shows the responsivity $R(\varepsilon)$ for the modes 20, 30, 40 and 60 for the pressure sweep device and for the model. Although higher modes have a higher slope, lower mode numbers show higher relative responsivities due to the lower frequency-level of the mode. For $\varepsilon > 0.1$, the data is in good agreement with the model, but for values $\varepsilon < 0.1$ the

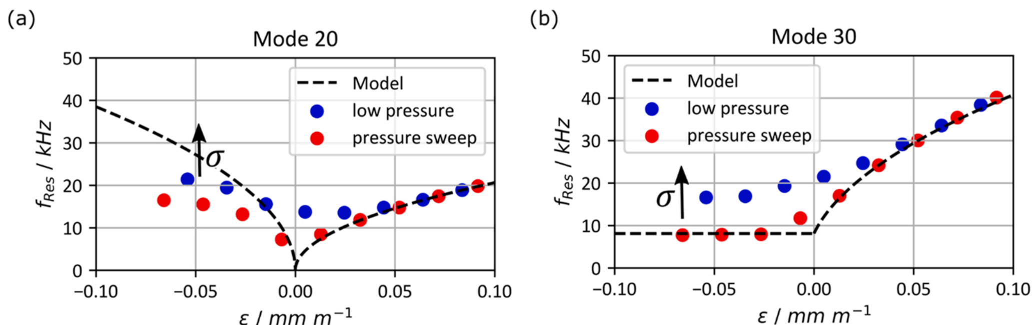

Fig. 11. Frequency of the resonance peaks for the 20-mode (a) and the 30-mode (b) for low-pressure and the pressure sweep sensor devices.

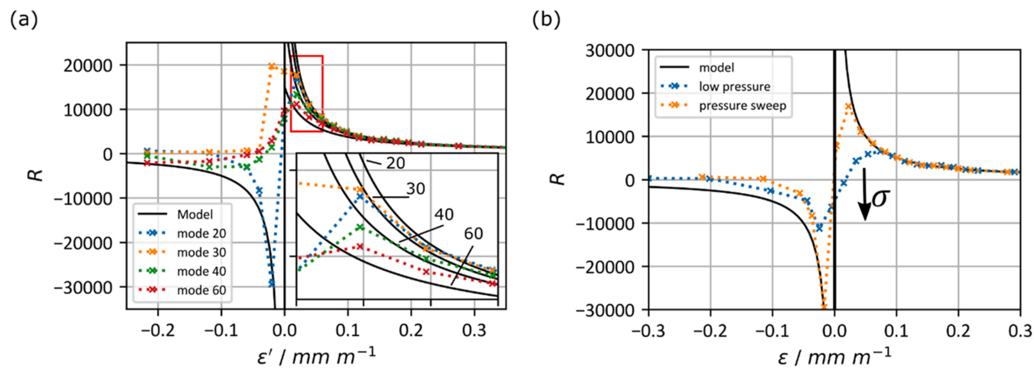

Fig. 12. (a) Responsivity of various modes for the pressure sweep device. (b) Comparison of the responsivity of the 20-modes for the low pressure and the pressure sweep device.

model diverges from the calculated data as the initial deflection is not incorporated in the model.

Fig. 12(b) shows the comparison of the mode 20 of the pressure sweep devices (orange), the low-pressure sample (blue) and the model (black). Similar to $f(\varepsilon)$ (compare Fig. 11) where the frequency at the critical strain value reached a lower minimum for devices with lower initial buckling or stress, the responsivity reaches a higher maximum. For the 20 mode this makes the pressure-sweep device more than twice as responsive as the low-pressure sample with $R_{pressure-sweep} \approx 17000$ compared to $R_{low-pressure} \approx 6500$.

Comparing our results with [75], where the devices were fabricated the same way as our low-pressure sample apart from different thicknesses for the deposited materials, we could increase the responsivity by a factor ~ 4.8 and ~ 1.8 for the pressure-sweep sample and the low-pressure sample, respectively. This increase comes from a combination of three factors. Beside the decreased intrinsic stress as explained before, the increased length and the decreased thickness of the beam directly increase the resonance frequencies of the microbridge in the base Eqs. (1) and (2) and hence the responsivity. The contributions of the increase in length from $1000\mu m$ to $1500\mu m$ and the decrease in thickness from $3\mu m$ to $1.6\mu m$ onto the responsivity can be estimated from Eqs. (1) and (11) and result in a factor of ~ 2. The reduced factor of 1.8 for the low-pressure sample most probably originates from the higher influence of the intrinsic stress on thinner and longer bridges, which results in a higher initial deflection and hence a lower responsivity for strain values close to ε_C. This shows that the device performance in case of a MEMS resonant strain sensor strongly depends on the residual stress and making it obvious that a sputter process for tailoring thin film stress is mostly needed.

5. Conclusion and outlook

In this study, a modified sputter process for stress-tailored AlN deposition with high piezoelectric constants is presented to improve the performance of a MEMS resonant strain sensing device which is sensible to buckling due to the intrinsic stress component. Various deposited AlN thin films were studied by characterizing their thin film morphology by XRD, SEM and AFM. The measurements showed that a pressure sweep starting from low-pressure of $0.2Pa$ and finishing at $0.6Pa$ supported by an AlN seed layer sputtered with $0.2Pa$ resulted in thin films which exhibit a reduced stress of $-170MPa$ compared to $-722MPa$ when deposited with standard conditions. Simultaneously, the piezoelectric coefficient d_{33} showed high values of $5.76pCN^{-1}$ which could not be reached with thin films sputtered only under high pressure of $0.6Pa$.

Subsequently, the low-pressure and the pressure-sweep thin films were used to fabricated MEMS resonant strain sensors and impact of intrinsic thin film stress component on the device performance were studied, by white light interferometric measurements and by characterizing the frequency responses as a function of external strain. The MEMS sensors fabricated with the stress reduced AlN thin film showed a responsivity of 17000 while the standard low-pressure sensor devices reached a corresponding value of 6500, which represents an increase by a factor of ~ 5. Compared to the latest results published in literature on resonant strain sensors both MEMS devices exceeded the responsivity of state-of-the-art sensors substantially, independent of their AlN fabrication route, demonstrating their outstanding performance for future low-power applications.

CRediT authorship contribution statement

M. Schlögl: Conceptualization, Methodology, Software, Formal analysis, Investigation, Writing – original draft, Visualization. **J. Weißenbach**: Formal analysis, Investigation. **M. Schneider**: Conceptualization, Methodology, Resources, Writing – review & editing, Supervision. **U. Schmidt**: Conceptualization, Resources, Writing – review & editing, Funding acquisition, Project administration, Supervision.

Declaration of Competing Interest

The authors declare that they have no known competing financial interests or personal relationships that could have appeared to influence the work reported in this paper.

Data availability

Data will be made available on request.

Acknowledgments

We greatly acknowledge the financial support by the FFG under contract number 865960/2018. The authors acknowledge TU Wien Bibliothek for financial support through its Open Access Funding Program.

References

[1] H. Noma, E. Ushijima, Y. Ooishi, M. Akiyama, N. Miyoshi, K. Kishi, T. Tabaru, I. Ohshima, A. Kakami, T. Kamohara, Adv. Mater. Res. 13–14 (2006) 111–116.
[2] K.S.A. Butcher, T.L. Tansley, J. Appl. Phys. 90 (2001) 6217–6221.
[3] X. Du, J. Zheng, U. Belegundu, K. Uchino, Appl. Phys. Lett. 72 (1998) 2421–2423.
[4] J.-S. Yang, S.-H. Kim, J.-H. Yeom, C.-Y. Koo, C.S. Hwang, E. Yoon, D.-J. Kim, J. Ha, Integr. Ferroelectr. 54 (2003) 515–525.
[5] T. Manzaneque, V. Ruiz-Díez, J. Hernando-García, E. Wistrela, M. Kucera, U. Schmid, J.L. Sánchez-Rojas, Sens. Actuators Phys. 220 (2014) 305–315.
[6] F. Patocka, C. Schneidhofer, N. Dörr, M. Schneider, U. Schmid, Sens. Actuators Phys. 315 (2020), 112290.
[7] F. Patocka, M. Schlögl, C. Schneidhofer, N. Dörr, M. Schneider, U. Schmid, Sens. Actuators B Chem. 299 (2019), 126957.
[8] P.M. Mayrhofer, C. Rehlendt, M. Fischeneder, M. Kucera, E. Wistrela, A. Bittner, U. Schmid, J. Micro Syst. 26 (2017) 102–112.

[9] S. Barth, H. Bartzsch, D. Glöß, P. Frach, T. Modes, O. Zywitzki, G. Suchaneck, G. Gerlach, Microsyst. Technol. 22 (2016) 1613–1617.
[10] R. Hou, D. Hutson, K.J. Kirk, Insight - Non-Destr. Test. Cond. Monit. 55 (2013) 302–307.
[11] L. Shu, X. Wang, L. Li, D. Yan, L. Peng, L. Fan, W. Wu, Sens. Actuators Phys. 293 (2019) 14–20.
[12] M. Schlögl, M. Schneider, U. Schmid, Mater. Sci. Eng. B 276 (2022), 115543.
[13] P.M. Mayrhofer, H. Riedl, H. Euchner, M. Stöger-Pollach, P.H. Mayrhofer, A. Bittner, U. Schmid, Acta Mater. 100 (2015) 81–89.
[14] M. Uehara, Y. Amano, S.A. Anggraini, K. Hirata, H. Yamada, M. Akiyama, Ceram. Int. 47 (2021) 16029–16036.
[15] M. Uehara, H. Shigemoto, Y. Fujio, T. Nagase, Y. Aida, K. Umeda, M. Akiyama, Appl. Phys. Lett. 111 (2017), 112901.
[16] V.V. Felmetsger, P.N. Laptev, S.M. Tanner, J. Vac. Sci. Technol. A 27 (2009) 417–422.
[17] M. Schneider, A. Bittner, U. Schmid, Appl. Phys. Lett. 105 (2014), 201912.
[18] M. Gillinger, M. Schneider, A. Bittner, P. Nicolay, U. Schmid, J. Appl. Phys. 117 (2015), 065303.
[19] N.R. Moody, D. Medlin, D. Boehme, D.P. Norwood, Eng. Fract. Mech. 61 (1998) 107–118.
[20] J. Olivares, E. Iborra, M. Clement, L. Vergara, J. Sangrador, A. Sanz-Hervás, Sens. Actuators Phys. 123–124 (2005) 590–595.
[21] K.E. Knisely, B. Hunt, B. Troelsen, E. Douglas, B.A. Griffin, J.E. Stevens, J. Micromech. Microeng. 28 (2018), 115009.
[22] H. Mehner, S. Leopold, M. Hoffmann, J. Micromech. Microeng. 23 (2013), 095030.
[23] R. Ali, M. Renzelli, M.I. Khan, M. Sebastiani, E. Bemporad, Nanomaterials 8 (2018) 896.
[24] A. Khandelwal, Z. Ren, S. Namiki, Z. Yang, N. Choudhary, C. Li, P. Wang, Z. Mi, X. Li, ACS Appl. Mater. Interfaces (2022).
[25] B. Ivira, R.Y. Fillit, F. Ndagijimana, P. Benech, J. Boussey, G. Parat, P. Ancey, J. Phys. Conf. Ser. 34 (2006) 668–673.
[26] B. Ivira, R.Y. Fillit, Ph Benech, F. Ndagijimana, G. Parat, P. Ancey, in: IECON 2006 - 32nd Annu. Conf. IEEE Ind. Electron., 2006, pp. 3133–3138.
[27] B.W. Sheldon, A. Rajamani, A. Bhandari, E. Chason, S.K. Hong, R. Beresford, J. Appl. Phys. 98 (2005), 043509.
[28] A. Pandey, S. Dutta, R. Prakash, S. Dalal, R. Raman, A.K. Kapoor, D. Kaur, Mater. Sci. Semicond. Process. 52 (2016) 16–23.
[29] (n.d.).
[30] L. Zhang, X. Zhang, J. Song, H. Zheng, Contin. Mech. Thermodyn. 32 (2020) 1127–1139.
[31] S. Fichtner, T. Reimer, S. Chemnitz, F. Lofink, B. Wagner, APL Mater. 3 (2015), 116102.
[32] K. Karakaya, M. Renaud, M. Goedbloed, R. van Schaijk, J. Micromech. Microeng. 18 (2008), 104012.
[33] S. Marauska, V. Hrkac, T. Dankwort, R. Jahns, H.J. Quenzer, R. Knöchel, L. Kienle, B. Wagner, Microsyst. Technol. 18 (2012) 787–795.
[34] S. Marauska, T. Dankwort, H.J. Quenzer, B. Wagner, Procedia Eng. 25 (2011) 1341–1344.
[35] H.-H. Lo, W.-L. Chen, P.J. Wang, W. Lai, Y.-K. Fuh, T.T. Li, Int. J. Adv. Manuf. Technol. (2022).
[36] (n.d.).
[37] E. Iborra, J. Olivares, M. Clement, L. Vergara, A. Sanz-Hervás, J. Sangrador, Sens. Actuators Phys. 115 (2004) 501–507.
[38] H.Y. Liu, G.S. Tang, F. Zeng, F. Pan, J. Cryst. Growth 363 (2013) 80–85.
[39] A. Assali, F. Laidoudi, R. Serhane, F. Kanouni, O. Mezilet, Mater. Today Commun. 26 (2021), 102067.
[40] A. Ababneh, U. Schmid, J. Hernando, J.L. Sánchez-Rojas, H. Seidel, Mater. Sci. Eng. B 172 (2010) 253–258.
[41] S. Dutta, A. Pandey, J. Mater. Sci. Mater. Electron. 32 (2021) 6705–6741.
[42] M.-A. Dubois, P. Muralt, J. Appl. Phys. 89 (2001) 6389–6395.
[43] T. Kamohara, M. Akiyama, N. Ueno, M. Sakamoto, K. Kano, A. Teshigahara, N. Kawahara, N. Kuwano, Appl. Phys. Lett. 89 (2006), 243507.
[44] T. Tabaru, M. Akiyama, Thin Solid Films 692 (2019), 137625.
[45] A.W. Leissa, J. Sound Vib. 31 (1973) 257–293.
[46] S. Bouwstra, B. Geijselaers, in: TRANSDUCERS 91 1991 Int. Conf. Solid-State Sens. Actuators Dig. Tech. Pap., 1991, pp. 538–542.
[47] M.A. Hopcroft, W.D. Nix, T.W. Kenny, J. Micro Syst. 19 (2010) 229–238.
[48] M.C. Salvadori, I.G. Brown, A.R. Vaz, L.L. Melo, M. Cattani, Phys. Rev. B 67 (2003), 153404.
[49] J. Lintymer, N. Martin, J.-M. Chappé, P. Delobelle, J. Takadoum, Surf. Coat. Technol. 200 (2005) 269–272.
[50] J.J. Wortman, R.A. Evans, J. Appl. Phys. 36 (1965) 153–156.
[51] J.G. Noel, IET Circuits Devices Syst. 10 (2016) 156–161.
[52] Mater. Prop. Database, 2022.
[53] Tilli Markku, et al.. Handbook of Silicon Based MEMS Materials and Technologies, 1st edition.,, Elsevier,, 2009.
[54] S. Venkataraj, D. Severin, R. Drese, F. Koerfer, M. Wuttig, Thin Solid Films 502 (2006) 235–239.
[55] M. Fischeneder, E. Wistrela, A. Bittner, M. Schneider, U. Schmid, Mater. Sci. Semicond. Process. 71 (2017) 283–289.
[56] M. Fischeneder, A. Bittner, M. Schneider, U. Schmid, Mater. Res. Express 5 (2018), 066412.
[57] Springerprofessional.De (n.d.).
[58] G.C.A.M. Janssen, M.M. Abdalla, F. van Keulen, B.R. Pujada, B. van Venrooy, Thin Solid Films 517 (2009) 1858–1867.
[59] M.B. Assouar, O. Elmazria, L. Le Brizoual, M. Belmahi, P. Alnot, in: Proc. 2002 IEEE Int. Freq. Control Symp. PDA Exhib. Cat No02CH37234, 2002, pp. 333–336.
[60] O. Elmazria, M.B. Assouar, P. Renard, P. Alnot, Phys. Status Solidi A 196 (2003) 416–421.
[61] H. Cheng, Y. Sun, P. Hing, Thin Solid Films 434 (2003) 112–120.
[62] T.P. Drüsedau, J. Bläsing, Thin Solid Films 377–378 (2000) 27–31.
[63] F. Hörich, R. Borgmann, J. Bläsing, G. Schmidt, P. Veit, F. Bertram, J. Christen, A. Strittmatter, A. Dadgar, J. Cryst. Growth 571 (2021), 126250.
[64] J.P. Kar, G. Bose, S. Tuli, Vacuum 81 (2006) 494–498.
[65] J.A. Pérez Taborda, J.C. Caicedo, M. Grisales, W. Saldarriaga, H. Riascos, Opt. Laser Technol. 69 (2015) 92–103.
[66] M.-C. Park, S.-W. Kim, Opt. Lett. 26 (2001) 420–422.
[67] A.W. Leissa, Z. Für, Angew. Math. Phys. ZAMP 25 (1974) 99–111.
[68] R.W. Claassen, C.J. Thorne, J. Aerosp. Sci. 29 (1962) 1300–1305.
[69] A.Z. Hajjaj, N. Alcheikh, M.I. Younis, , Int. J. Non-Linear Mech. 95 (2017) 277–286.
[70] N. Alcheikh, A.Z. Hajjaj, M.I. Younis, Sens. Actuators Phys. 300 (2019), 111652.
[71] A.R. Behera, H. Shaik, G.M. Rao, R. Pratap, J. Micro Syst. 28 (2019) 1039–1054.
[72] X. Song, H. Liu, in: American Society of Mechanical Engineers Digital Collection, 2020.
[73] H. Wang, X. Ning, H. Li, H. Luan, Y. Xue, X. Yu, Z. Fan, L. Li, J.A. Rogers, Y. Zhang, Y. Huang, J. Mech. Phys. Solids 112 (2018) 187–208.
[74] A.H. Nayfeh, W. Kreider, T.J. Anderson, AIAA J. (2012).
[75] M. Schlögl, S. Köppl, J. Hiesberger, M. Schneider, U. Schmid, unpublished (2022).

Matthias Schlögl received his Bachelor and master's degree in electrical engineering from TU Wien in 2015 and 2018, respectively. He is currently working on his Ph.D. thesis on materials and devices for piezoelectric energy harvesting and resonant strain sensing at the Department of Microsystems Technology at TU Wien.

J. Weißenbach received his Bachelor and master's degree in electrical engineering from TU Wien in 2018 and 2021, respectively. From 2018–2020 he was working as an assistant at the Institute of Sensor and Actuator Systems and collected practical lab experience.

M. Schneider studied physics at the Karlsruhe Institute of Technology 2003–2009. He performed his diploma work at the Forschungszentrum Karlsruhe on the measurement of Lorentz angles in highly irradiated silicon strip detectors for high energy collider applications such as the large hadron collider at CERN. He finished his studies in 2009 and started his Ph.D. thesis on the optimization of ultra-thin aluminum nitride films for actuation and sensing applications at the Department of Microsystems Technology at TU Wien. He received his Ph.D. in 2014 and is currently working as assistant professor on the topic of advanced piezoelectric microsystems.

Ulrich Schmid started studies in physics and mathematics in 1992. He performed his diploma work at the research laboratories of the Daimler–Benz AG on the electrical characterization of silicon carbide microelectronic devices for high temperature applications. In 1999, he joined the research laboratories of Daimler–Chrysler AG (now Airbus Group) in Ottobrunn/Munich. He developed a robust fuel injection rate sensor for automotive diesel engines and received his Ph.D. degree in 2003. From 2003–2008, he was a post-doc at the Chair of Micromechanics, Microfluidics/Microactuators at Saarland University. Since October 2008, he is a full professor for Microsystems Technology at TU Wien.